AIAA SciTech Forum
7-11 January 2019, San Diego, California
AIAA Scitech 2019 Forum

10.2514/6.2019-2137

Direct numerical simulation of random rough surfaces in turbulent channel flow

Rong Ma* and Karim Alamé†
Aerospace Engineering and Mechanics, University of Minnesota, Minneapolis, MN, 55455, USA

Krishnan Mahesh‡
Aerospace Engineering and Mechanics, University of Minnesota, Minneapolis, MN, 55455, USA

Direct numerical simulation (DNS) is performed to study the effects of random rough surfaces on the flow field in a turbulent channel flow at $Re_\tau = 400$. The rough surface tiles generated synthetically from a prescribed energy spectrum using a power-law are provided by Flack and Schultz (personal communication). The rough surface is applied on the bottom wall only. The skin friction coefficient of the rough wall shows good agreement with the experimental results from Flack and Schultz. The turbulent statistics are compared to DNS results of the turbulent smooth channel flow. A velocity deficit is observed in the log-law region, indicating an increased drag due to roughness. Streamwise (x) and spanwise (z) velocity fluctuations are enhanced in the near-wall region. The pressure fluctuations are larger in the roughness sublayer when compared to a smooth channel flow. The mean momentum balance (MMB) is examined using the ratio of the viscous stress gradient to the Reynolds stress gradient. The results demonstrate that the qualitative features of the MMB layer of the smooth wall are maintained for the rough wall. The peak Reynolds stress location y_p shifts closer to the wall and is less than $y^+ = 40$ (y_p of a smooth channel case). DNS of a rod-roughened channel flow is also performed for comparison. The probability density function (PDF) distribution of the streamwise and spanwise wall shear-stress components τ_{yx} and τ_{yz} for the rod-roughened and the random rough surface exhibits higher kurtosis than the smooth case. This implies that the probability of extreme events is higher for rough walls. For the rod-roughened case, the joint PDF distribution indicates the dominance of recirculation zones between adjacent rods. For the random rough surface, the presence of valleys leads to reverse flows near the roughness elements, however, they are not as strong as the recirculation zones in the rod-roughened case.

I. Nomenclature

Re_τ	=	Friction Reynolds number
u_τ	=	Friction velocity
C_f	=	Skin friction coefficient
y_p	=	Peak Reynolds stress location
τ_{yx}	=	Streamwise wall shear-stress component
τ_{yz}	=	Spanwise wall shear-stress component
N_x, N_y, N_z	=	Number of computational cells in streamwise, wall-normal, and spanwise direction
L_x, L_y, L_z	=	Length, height, and width of the channel
$\Delta x^+, \Delta y^+, \Delta z^+$	=	Streamwise, wall-normal, and spanwise grid spacing in wall units
h	=	Roughness height
k_{rms}	=	Root-mean-square roughness height
k_s	=	Equivalent sandgrain roughness height
ES	=	Effective slope

*Graduate Research Assistant, Aerospace Engineering and Mechanics, University of Minnesota
†Graduate Research Assistant, Aerospace Engineering and Mechanics, University of Minnesota
‡Professor, Aerospace Engineering and Mechanics, University of Minnesota, and AIAA Associate Fellow

U_0	=	Centerline velocity
$< U >$	=	Average streamwise velocity
$< U >^+$	=	Average streamwise velocity normalized by u_τ
$< u_i' u_j' >^+$	=	Reynolds stresses normalized by u_τ^2
p_{rms}	=	Root-mean-square pressure fluctuations
λ	=	Roughness pitch
δ	=	Channel half-height
δ_t	=	Effective layer thickness

II. Introduction

The effect of roughness on turbulent flows is of great interest due to its impact on skin friction and pressure drag which can modify near-wall flow structures. A recent review by Flack and Schultz [1] discusses the different methods to predict skin friction drag on rough surfaces. The correlations and scaling parameters based on regular surfaces are summarized and their limitations are highlighted in the context of irregular rough surfaces. New correlations are proposed to better predict the effect of realistically rough surfaces on the flow field. They found that the equivalent sandgrain roughness height k_s is an important parameter to collapse the roughness function of a wide range of roughness types in a fully rough regime. A new roughness correlation is provided by Flack and Schultz [1], which indicates that the root-mean-square roughness height k_{rms} and the skewness have the strongest correlations with k_s. Yuan and Piomelli [2] conducted large-eddy simulations (LES) of flow over realistic surfaces and found that the effective slope (ES) is an additional important parameter when the surface is not sufficiently steep. Busse et al. [3] used DNS to simulate the flow over a realistically rough surface based on a surface scan. The influence of small scale surface features on the turbulent flow field was investigated by using a low-pass Fourier filter on the surface roughness. Their results show that the mean flow and turbulent statistics change noticeably when a very low cut-off number is used. Mehdi et al. [4] presented the analysis of the mean momentum balance (MMB) for rough-wall turbulent boundary layers. They showed a collapse in the data when the viscous to Reynolds stress gradient ratio was normalized by the peak Reynolds stress location y_p. Bhaganagar et al. [5] investigated the increased form drag as a result of a regular array of "egg-carton" shaped roughness elements on the bottom wall of a turbulent channel. They found that the increased form drag is associated with more intense pressure fluctuations. Meyers et al. [6] performed measurements of wall-pressure spectrum on a series of high-Reynolds-number turbulent boundary layer over rough surfaces. Many different scalings were investigated but no universal scaling law was found to collapse the whole range of frequencies. The wall shear stress is directly related to the skin friction drag. Diaz-Daniel et al. [7] investigated the probability distribution of the smooth wall shear-stress fluctuations and found that while the signal of τ_{yx} has positive skewness, the fluctuations of τ_{yz} are zero-skewed. They also suggested that for different Reynolds numbers, a better collapse is obtained through normalizing the PDF by subtracting the mean and dividing by the root mean square of the corresponding shear stress. Khoo et al. [8] performed experiments on a smooth turbulent channel flow using hot-wire probes near the wall. The PDF results suggest that the streamwise wall shear-stress component is correlated with the streamwise velocity fluctuations in the viscous sublayer. The time history of τ_{yx} indicates that the large-scale peaks contribute to the high values of skewness and flatness.

The purpose of the present study is to perform DNS of turbulent channel flow for a rod-roughened case and a random rough surface. We investigate the effect of roughness on drag, turbulent statistics, near-wall flow field and wall shear-stress fluctuations. The results are compared to a baseline smooth channel flow.

III. Simulation details

A. Numerical method

Direct numerical simulation (DNS) is performed to study the effects of a realistically rough surface on the flow field. The governing equations are solved using the finite volume algorithm developed by Mahesh et al. [9]. The governing equations for the momentum and continuity equations are given by the Navier-Stokes equations:

$$\frac{\partial u_i}{\partial t} + \frac{\partial}{\partial x_j}(u_i u_j) = -\frac{\partial p}{\partial x_i} + \nu \frac{\partial}{\partial x_j}\left(\frac{\partial u_i}{\partial x_j} + \frac{\partial u_j}{\partial x_i}\right) + K_i, \tag{1}$$

$$\frac{\partial u_i}{\partial x_i} = 0, \tag{2}$$

where u_i and x_i are the i-th component of the velocity and position vectors respectively, p denotes pressure, ν is the kinematic viscosity of the fluid and K_i is the body force. The algorithm is robust and emphasizes discrete kinetic energy conservation in the inviscid limit which enables it to simulate high-Reynolds number flows without adding numerical dissipation. The solution is advanced implicitly in time using an SOR method. A predictor-corrector methodology is used where the velocities are first predicted using the momentum equation, and then corrected using the pressure gradient obtained from the Poisson equation yielded by the continuity equation. The Poisson equation is solved using a multigrid pre-conditioned conjugate gradient method (CGM) using the Trilinos libraries (Sandia National Labs). The implicit time advancement uses the Crank-Nicholson discretization with a linearization of the convective terms.

The surface is represented by obstacle cells which are masked out. Fluid cells are flagged as $mask = 1$ and obstacle cells as $mask = 0$. The wetted masked cells (cells that share a face between a fluid and obstacle cell) enforce a zero face-normal velocity $v_N|_{mask} = 0$. The cell-centered velocities satisfy a no-slip boundary condition, with the exception of corner cells that take a weighted average of the neighboring cell-centered values.

B. Validation

The DNS code is validated against Moser et al. [10] for the smooth channel flow at $Re_\tau = 400$ and Ashrafian et al. [11] for the pressure-driven turbulent flow in a rod-roughened channel at $Re_\tau = 400$. The grid details are outlined in Table 1. The smooth channel flow is denoted by Case SW, and the rod-roughened channel flow is denoted by Case RRW. For Case SW, the mean velocity profile and Reynolds stresses are shown in Fig. 1. For Case RRW, both the top and bottom walls are roughened by 24 square rods with a height of 1.7% of the channel height. Figure 2(a) shows the defect profiles scaled with the centerline velocity U_0. The variation of the Reynolds stresses normalized by u_τ^2 at slice $x/\lambda = 0.312$ are plotted from the wall to the centerline using outer layer coordinates in Fig. 2(b). Both velocity and intensity profiles show good agreement.

Table 1 Simulation parameters for DNS of the validation cases.

Turbulent channel flow	Case	Re_τ	$Nx \times Ny \times Nz$	$Lx \times Ly \times Lz$	Δx^+	Δz^+	Δy^+_{min}	Δy^+_{max}
Smooth wall	SW	400	$768 \times 320 \times 384$	$2\pi \times 2.03 \times \pi$	3.27	3.27	0.85	5.48
Rod-roughened wall	RRW	400	$768 \times 320 \times 320$	$6.528 \times 2 \times \pi$	3.40	3.92	0.85	5.48

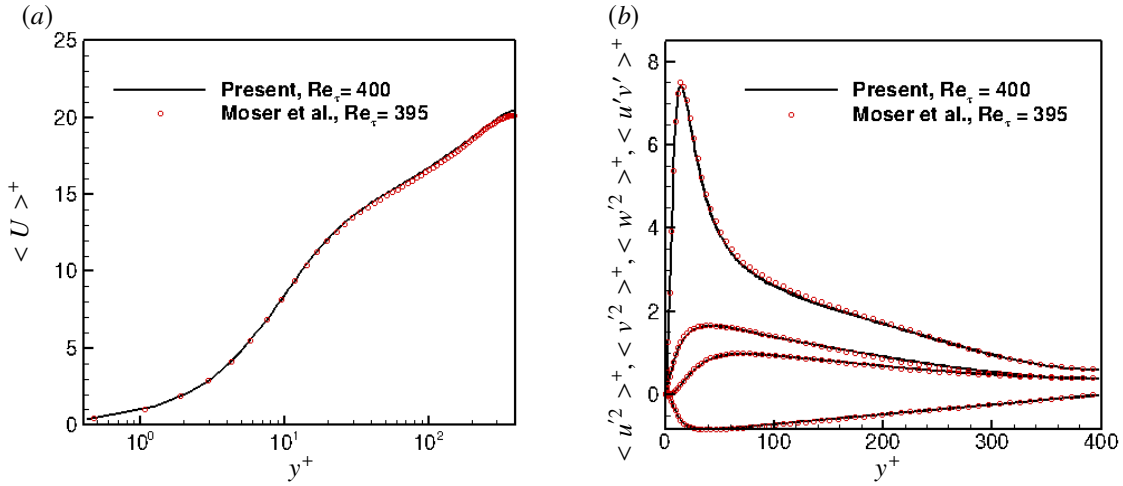

Fig. 1 DNS of a smooth channel flow at $Re_\tau = 400$ compared to the DNS of Moser et al. [10]: (a) Mean velocity profile; (b) Reynolds stresses in inner layer coordinate.

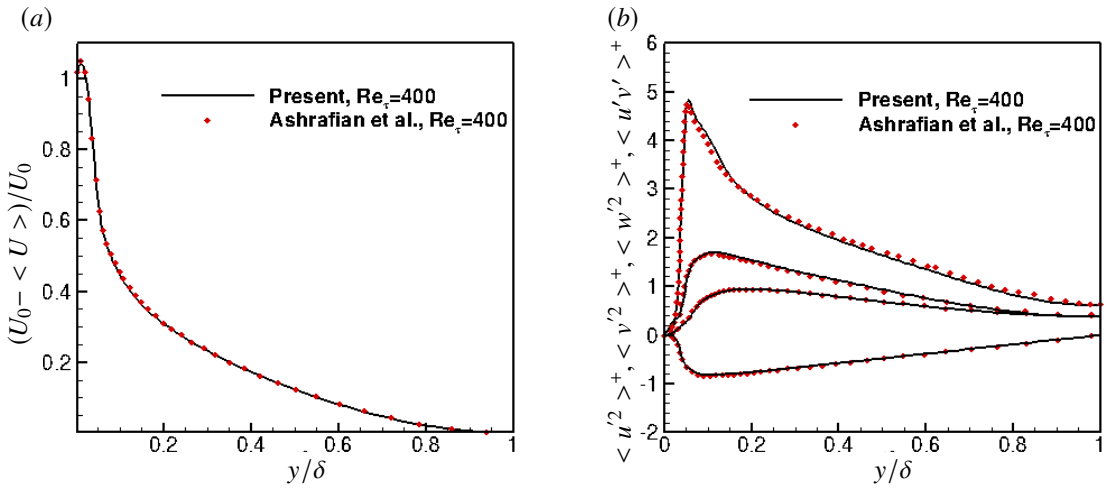

Fig. 2 DNS of a rod-roughened channel flow at $Re_\tau = 400$ compared to the DNS of Ashrafian et al. [11]: (a) The defect profiles scaled with centerline velocity U_0 at $x/\lambda = 0.312$; (b) Reynolds stresses in outer layer coordinate at $x/\lambda = 0.312$.

C. Computational Setup

1. Processing the surface data

The rough surface tiles are provided by Flack and Schultz (personal communication), which have a k_{rms} value around $100\mu m$. The details of surface generation are presented in Barros et al. [12]. Each surface tile is originally resolved using 3534×1016 points, which is interpolated onto grids of size 489×123. Then, the rough surface over the bottom wall is made up by rotating each generated section in a random orientation and tiled to achieve a horizontal domain of size $2\pi\delta \times \pi\delta$, where δ is the channel half-height.

The characteristic parameters of the rough surface after processing are compared to those of the original tiles, shown in Table 2. The results show a good agreement. The probability density function (PDF) distributions of the processed rough surface and the original tile are compared in Fig. 3(a), and good agreement is obtained. Figure 3(b) provides an illustration of the rough surface coloured with height.

Table 2 Statistics of the original tiles and the processed rough surface in the present work.

Parameter (mm)	Description	Tile 1	Tile 2	Tile 3	Tile 4	Average	Rough surface
k_a	Average Roughness Height	0.0691	0.0698	0.0700	0.0718	0.0702	0.0692
k_{rms}	RMS Roughness Height	0.0862	0.0875	0.0878	0.0892	0.0877	0.0865
k_t	Maximum Peak to Valley Height	0.703	0.692	0.696	0.729	0.705	0.745
Sk	Skewness	-0.021	-0.083	-0.073	-0.080	-0.064	-0.053
Ku	Kurtosis (Flatness)	2.932	2.985	2.974	2.812	2.926	2.933
ES_x	RMS Slope of Roughness in x	0.360	0.390	0.372	0.370	0.373	0.265
ES_y	RMS Slope of Roughness in y	0.359	0.392	0.370	0.371	0.373	0.265

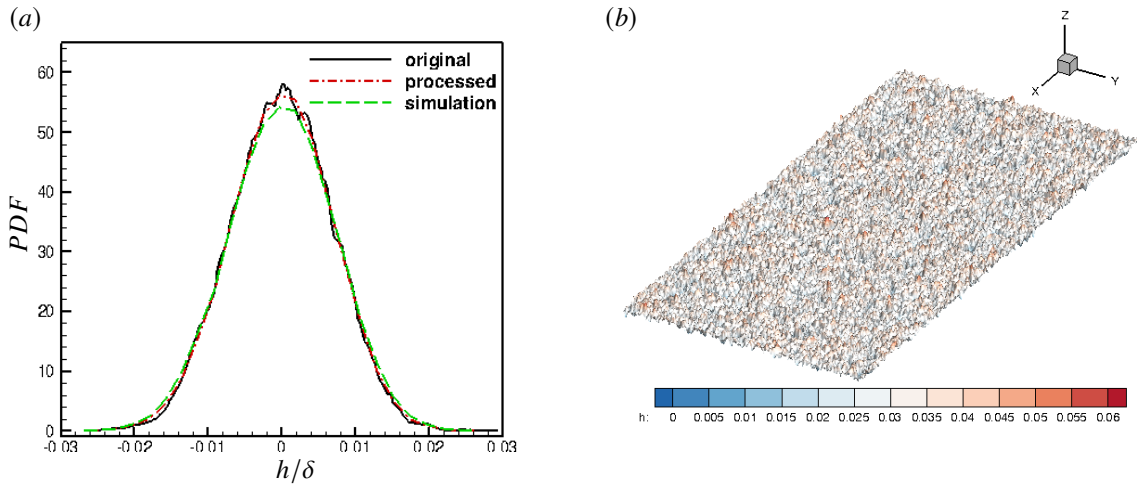

Fig. 3 (a) The probability density function (PDF) distribution of the height normalized by the channel half-height δ for the processed rough surface compared to the original surface tile; (b) Illustration of the rough surface. The contour legend describes the height of the surface profile normalized by δ.

2. Problem Setup

A channel flow is simulated with no-slip boundary conditions at the wall and periodic boundary conditions in the streamwise and spanwise directions. Non-uniform grids are used in the wall-normal direction while uniform grids are used in both the streamwise and spanwise directions. The rough surface is applied on the bottom wall only and Reynolds number, mesh size, domain length and mesh resolution in viscous wall units are shown in Table 3. The random rough case is denoted by Case $k_{rms} - 100$. The equivalent sandgrain roughness height in wall units k_s^+ is equal to 5.12.

Table 3 Simulation parameters for DNS of the random rough surface case.

Turbulent channel flow	Case	Re_τ	$Nx \times Ny \times Nz$	$Lx \times Ly \times Lz$	Δx^+	Δz^+	Δy^+_{min}	Δy^+_{max}
Random rough wall	$k_{rms} - 100$	400	$768 \times 320 \times 322$	$2\pi \times 2.03 \times \pi$	3.27	3.90	0.85	5.64

IV. Results

A. Instantaneous flow field

The instantaneous streamwise velocity contours at $x = \pi$ are shown in Fig. 4(a)-(d). Figure 4(a) shows the instantaneous velocity contours at $y^+ = 2$. The velocity field is quiescent in the near-wall region. Figure 4(b) shows contours of the vorticity magnitude at $y^+ = 2$. Large regions of high vorticity are observed at certain locations near the roughness asperities. Figure 4(c) and (d) illustrate the instantaneous velocity field and the vorticity magnitude respectively at $y^+ = 4$. Larger streaks are visible which indicate that the flow field is less quiescent in that region when compared to the contours at $y^+ = 2$.

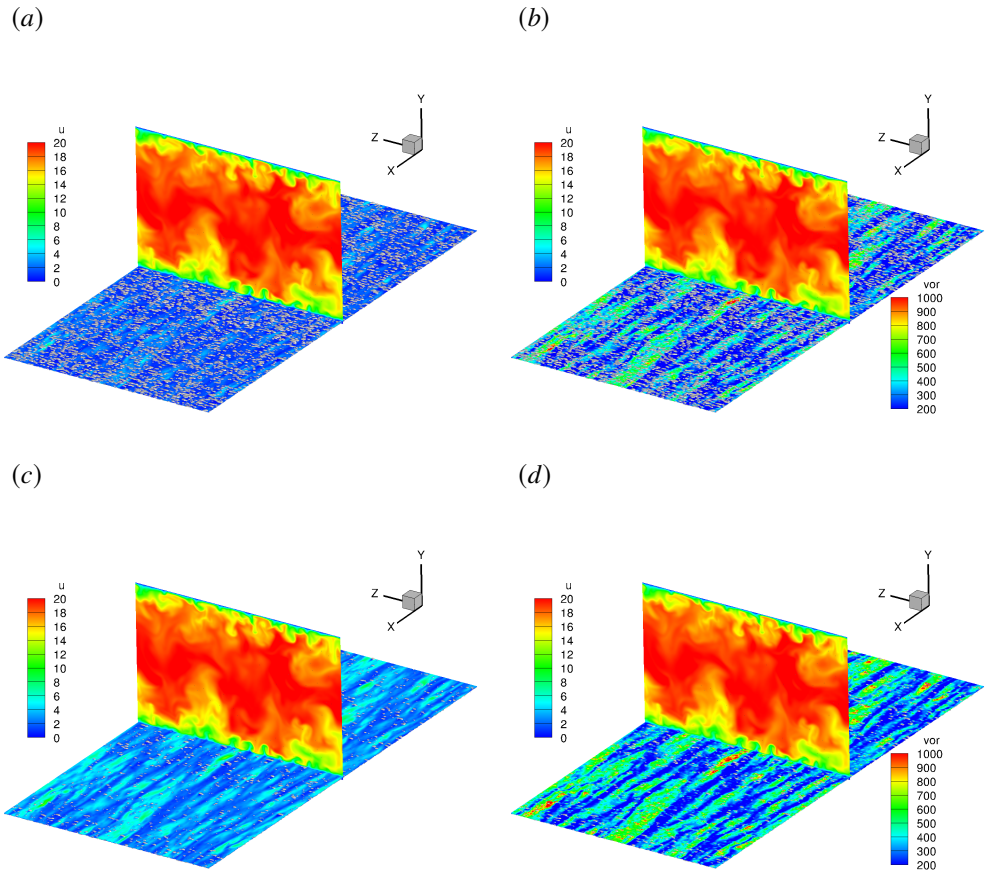

Fig. 4 Planar plots for Case $k_{rms} - 100$ with streamwise velocity contours at $x = \pi$ for all sub-figures; (a) The streamwise velocity and (b) the magnitude of vorticity at y-plane location of $y^+ = 2$; (c) The streamwise velocity and (d) the magnitude of vorticity at y-plane location of $y^+ = 4$.

B. Mean flow field

1. Skin friction, mean velocity and velocity fluctuations

The shear stress over the bottom rough wall of Case $k_{rms} - 100$ is computed from the force balance between the drag and body force. The skin friction coefficient of the rough wall is 0.0073 at the corresponding Reynolds number $Re_\tau = 400$, which have a good agreement with the experimental result 0.0072 from Flack and Schultz. The mean velocity profiles and velocity fluctuations of Case $k_{rms} - 100$ are compared to the smooth channel flow at $Re_\tau = 400$ of Moser et al. [10] in Fig. 5(a) and (b). A mean velocity deficit is observed in the log-law region indicating an increase in drag due to the presence of roughness. The Reynolds stresses of the top wall are scaled by smooth-wall friction velocity $u_{\tau,t}$ where $u_{\tau,t} = 0.980$, while the Reynolds stresses of bottom wall are scaled by rough-wall friction velocity $u_{\tau,b}$ where $u_{\tau,b} = 1.019$. The roughness does not affect velocity fluctuations as much since the fluctuation peak value occurs above the roughness sublayer. The peak of streamwise velocity fluctuations for the top wall matches with the smooth channel case of Moser et al. [10], while the peak for the bottom wall is lower.

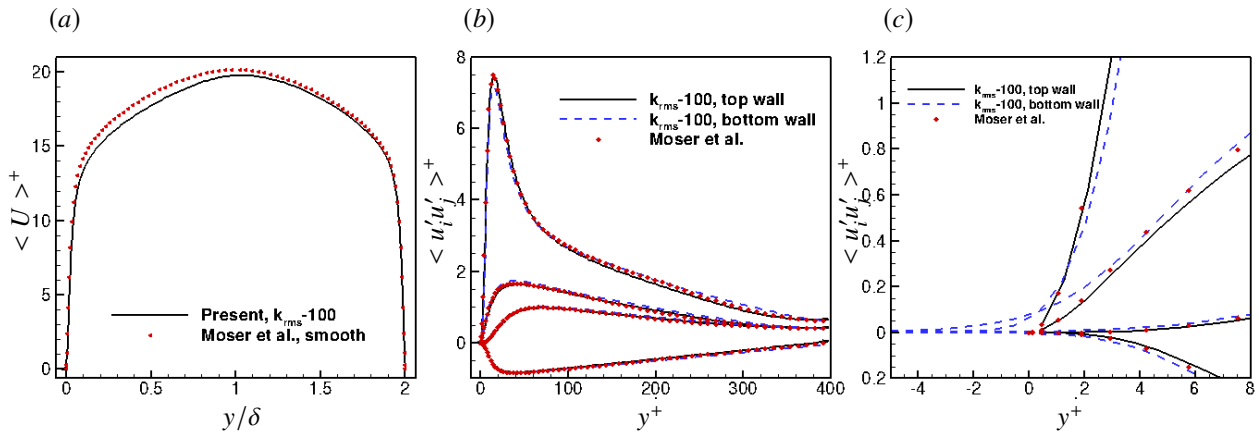

Fig. 5 Random rough channel flow of Case $k_{rms} - 100$: (a) Mean velocity profile in outer layer coordinate; (b) Velocity fluctuations in inner layer coordinate, top wall normalized by $u^2_{\tau,t}$, bottom wall normalized by $u^2_{\tau,b}$; (c) Zoom-in plot of velocity fluctuations in the near-wall region.

In the near-wall region, there is a higher level of velocity fluctuations for the rough surface compared to the smooth turbulent channel flow of Moser et al. [10]. Streamwise and spanwise components have higher fluctuation levels, as shown in Fig. 5 (c). Instantaneous velocity fields in Fig. 6 are shown at wall-normal location $y^+ = 2$. Similar features of higher velocity fluctuations are observed in streamwise and spanwise components than the wall-normal component.

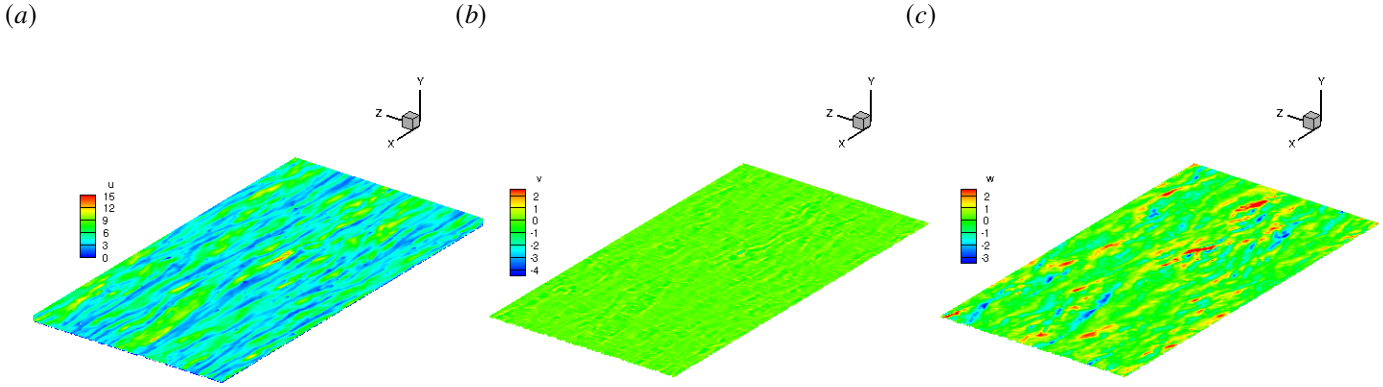

Fig. 6 Inner layer velocity fluctuations for Case $k_{rms} - 100$: (a) streamwise, (b) wall-normal, and (c) spanwise instantaneous velocity field at $y^+ = 2$.

2. Pressure fluctuations

The root-mean-squared (RMS) pressure fluctuations p^+_{rms} for Case $k_{rms} - 100$ are compared to Case SW and the smooth channel flow of Moser et al. [10] at $Re_\tau = 400$. In the roughness sublayer ($y^+ < 12$), the pressure fluctuations are enhanced by the roughness. The p^+_{rms} profile maintains the same features as those for the smooth wall in the outer layer region ($y^+ > 12$). The result is shown in Fig. 7.

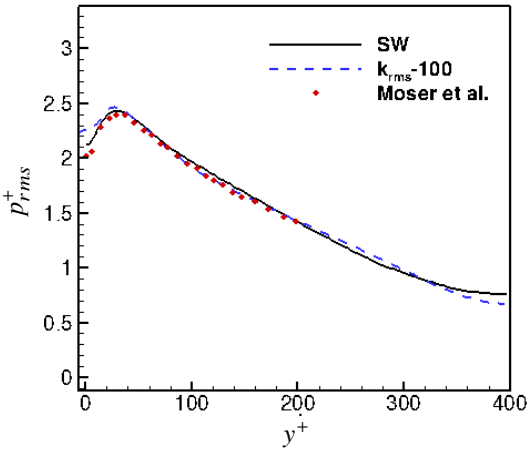

Fig. 7 RMS pressure fluctuations of Case $k_{rms} - 100$ scaled by rough-wall friction velocity $u_{\tau,b}$.

The top view of the pressure field in x-z plane is shown in Fig. 8 at different cut planes in the wall-normal direction at $y^+ = 2$ and $y^+ = 4$. The asperities are visible and their effect on form drag is evident from the pressure fluctuations in the wake of each roughness element. As the height of the cut plane is increased in the wall-normal direction, the effect of roughness is reduced. This can be seen in Fig. 8 (a) and (b).

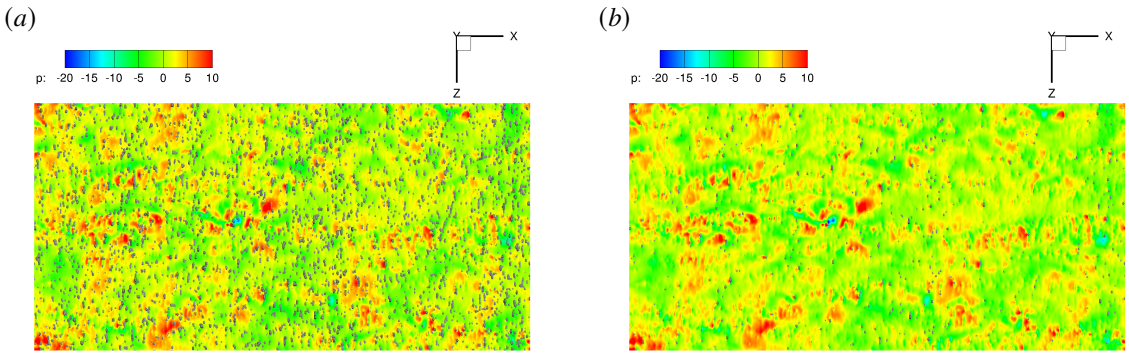

Fig. 8 Pressure field in x-z plane for Case $k_{rms} - 100$: (a) wall-normal location $y^+ = 2$; (b) $y^+ = 4$.

C. Momentum Budget

An effective layer thickness δ_t is defined for the half channel with the rough wall based on the distance from the virtual origin (mean height location $y_0 = 0.03$) to the location of the maximum mean velocity $y_m = 1.064$. The wall-normal location is therefore shifted by $y_{shift} = (y - y_0)/\delta_t$, where the symbol y denotes the wall-normal location normalized by channel half-height δ, and $\delta_t = y_m - y_0$.

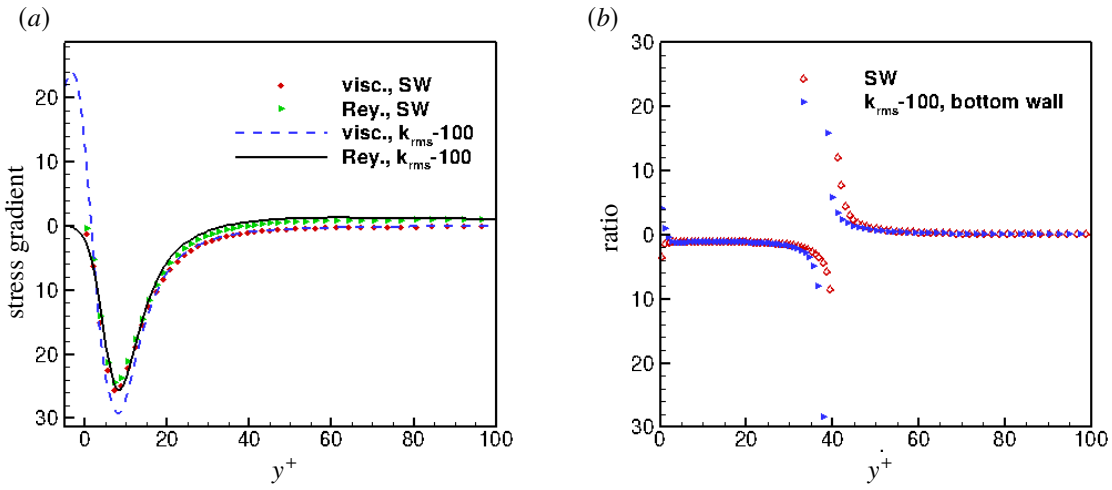

Fig. 9 Mean momentum balance in inner layer coordinate: (a) Viscous stress gradient and Reynolds stress gradient; (b) Ratio of the viscous to Reynolds stress gradients for Case SW, and Case $k_{rms} - 100$ at $Re_\tau = 400$.

The viscous stress gradient and the Reynolds stress gradient for Case SW and Case $k_{rms} - 100$ are plotted in Fig. 9(a). In the region $y^+ < 5$, the viscous stress gradient of Case $k_{rms} - 100$ shows high values while the viscous stress gradient of Case SW maintains small value. This indicates the frictional drag is increased by the roughness in the roughness sublayer. The peak of viscous and Reynolds stress gradients for both cases are shown at $y^+ = 7$. The peak values of stress gradients for Case $k_{rms} - 100$ are higher than those for Case SW. When $y^+ > 10$, no appreciable difference is observed in stress gradients between the smooth and rough walls. Figure 9(b) demonstrates that Case $k_{rms} - 100$ maintains similar properties of the MMB layer structure with the smooth wall. A positive large ratio value occurs in the near-wall region due to the presence of roughness. The peak Reynolds stress location y_p is at $y^+ = 40$ for the smooth wall, which denotes the transition from a balance between mean viscous force and mean effect of turbulent inertia to a balance between mean effect of turbulent inertia and mean advection. Roughness causes the transition to occur closer to the wall when compared to a smooth case.

D. The statistics of wall shear-stress fluctuations

Consider that the flow features within the groove and outside of the groove are different, the projected surfaces are divided into two separate regions. For Case RRW, the first region is the top surface of the rod, the second region is the bottom surface within the cavity between the rods. The wall shear-stress signals are probed separately in those two regions. Similarly, for Case $k_{rms} - 100$, the mean height location of the roughness is chosen to be the reference plane. The surface is divided into the peak region, which is above the mean height location, and the valley region, which is below the mean height location. The schematic diagram is shown in Fig. 10.

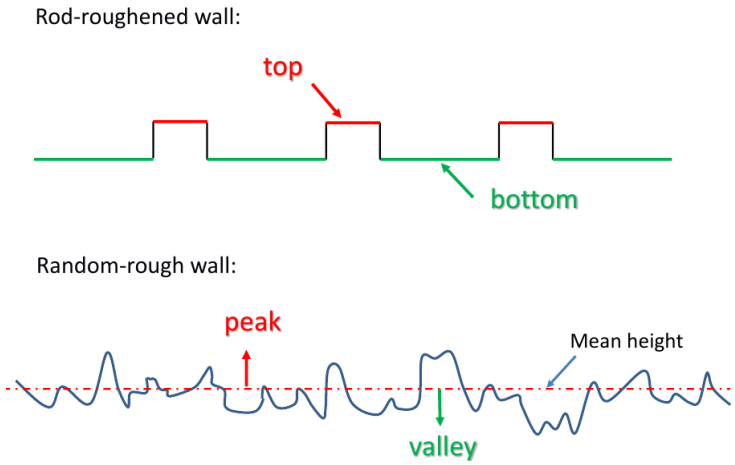

Fig. 10 Sketch of data probe for wall shear-stress fluctuations

1. PDF distribution of wall shear stress

The PDF of Case SW at $Re_\tau = 400$ match with Diaz-Daniel et al. [7]. The PDF distributions of the streamwise shear stress component τ_{yx}, spanwise shear stress component τ_{yz} and the shear-stress yaw angle ϕ_τ for rod-roughened and random rough channel flows are investigated and compared to the baseline smooth channel case. The statistical properties of the wall shear-stress fluctuations are shown in Table 4.

Case SW shows that the PDF profile of τ_{yx} has positive skewness and follows a near log-normal distribution. The kurtosis $Ku = 4.50$ is larger than a normal Gaussian distribution with $Ku = 3$. Compared to the smooth case, shown in Fig. 11(a), the top surface of the rod-roughened wall maintains larger magnitudes and positive values of mean and skewness. The bottom of the cavity has a negative mean value and negative skewness. This is due to the fact that two recirculating zones fill up most of the cavity region, as shown in Fig. 12(a). A large separation is formed downstream of the rod, whereas a smaller vortex is located upstream of the adjacent rod. The kurtosis of τ_{yx} has a higher value, meaning that the extreme events have a higher probability. For Case $k_{rms} - 100$, the signals of τ_{yx} are positive-skewed for both peak and valley regions. The mean value of τ_{yx} in the valley region is relatively small. This is due to the reverse flow induced by the presence of the roughness elements, as shown in Fig. 12(b). The kurtosis of τ_{yx} is even higher than the rod-roughened case, indicating that the extreme events have higher probability for the random rough case.

The spanwise shear-stress fluctuations of τ_{yz} have zero mean values and are zero-skewed for smooth, rod-roughened, and random rough cases. The PDF distribution of τ_{yz} is shown in Fig. 11(b). For Case RRW, the kurtosis of the top surface has the same value as the smooth wall, whereas the kurtosis of the bottom surface is larger. The kurtosis of τ_{yz} for Case $k_{rms} - 100$ is also greater than the rod-roughened case. The bottom surface of rod-roughened wall and the valley region of random rough wall have larger kurtosis than the top surface and the peak region, indicating that the higher probability of extreme events are likely caused by the presence of cavities and valleys.

The probability distribution of the shear-stress yaw angle $\phi_\tau(t) = \tan^{-1}(\tau_{yz}(t)/\tau_{yx}(t))$ is shown in Fig. 11(c). For smooth channel flows, Jeon et al. [13] found that the probability for events with the magnitude of shear-stress yaw angle greater than $45°(|\phi_\tau| > 45°)$ is very small. This means that the high, positive streamwise fluctuations τ_{yx} are associated with relatively small spanwise fluctuations τ_{yz}. Compared to Case SW, the standard deviation of ϕ_τ is much higher for two rough cases. The probability of events with $45° < |\phi_\tau| < 90°$ is enhanced by the roughness, indicating that the events with the relatively small fluctuations τ_{yx} related to larger spanwise fluctuations τ_{yz} have a higher probability. These results are consistent with the findings in the instantaneous streamwise velocity field, where the streaks are found to be broken up by the roughness elements. The PDF profiles of the top surface and the peak region show similar properties, while the bottom surface and the valley region have different distributions. The events for $90° < |\phi_\tau| < 180°$ have a higher probability for the bottom surface in Case RRW when compared to the smooth wall. These events correspond to the negative value of τ_{yx}, which imply that the flow features are strongly dominated by

the recirculation zones in the cavity. The valley region in Case $k_{rms}-100$ is more evenly distributed when compared to the smooth wall case. For $|\phi_\tau| < 20°$, the probability of events for Case SW is much larger than Case $k_{rms}-100$. This event represents large values of τ_{yx} correlated with small values of τ_{yz}. For $|\phi_\tau| > 45°$, the probability of events for Case SW is negligible when compared to Case $k_{rms}-100$. This event represents smaller or equal values of τ_{yx} correlated with τ_{yz}. This implies that the presence of valleys breaks up the directional bias of the streamwise wall shear-stress fluctuations. The increased probability of occurrences with the yaw angle between 90° and 180° illustrates that the flow reversals are enhanced in the valleys, however, they are not as strong as the recirculation zones between the rods where the probability for Case RRW is larger.

Table 4 Statistics of the wall shear-stress components τ_{yx}, τ_{yz} and yaw angle ϕ_τ: mean $\mu(\cdot)$, skewness $Sk(\cdot)$, kurtosis $Ku(\cdot)$, standard deviation $\sigma(\cdot)$ for smooth, rod-roughened and random rough channel flow at $Re_\tau = 400$.

Case	$\mu(\tau'_{yx})$	Sk(τ'_{yx})	Ku(τ'_{yx})	$\mu(\tau'_{yz})$	Sk(τ'_{yz})	Ku(τ'_{yz})	$\sigma(\phi_\tau)$
SW	1.09	0.97	4.50	1.45e-2	-0.18	8.79	14.54
RRW, top	1.89	1.79	7.30	-3.48e-3	5.77e-2	8.72	25.01
RRW, bottom	-0.27	-2.03	11.56	-2.10e-3	2.45e-2	10.86	138.07
$k_{rms}-100$, peak	1.34	2.21	11.00	3.95e-3	-1.28e-2	10.09	32.52
$k_{rms}-100$, valley	0.21	2.22	13.09	-7.11e-3	-0.17	14.72	80.65

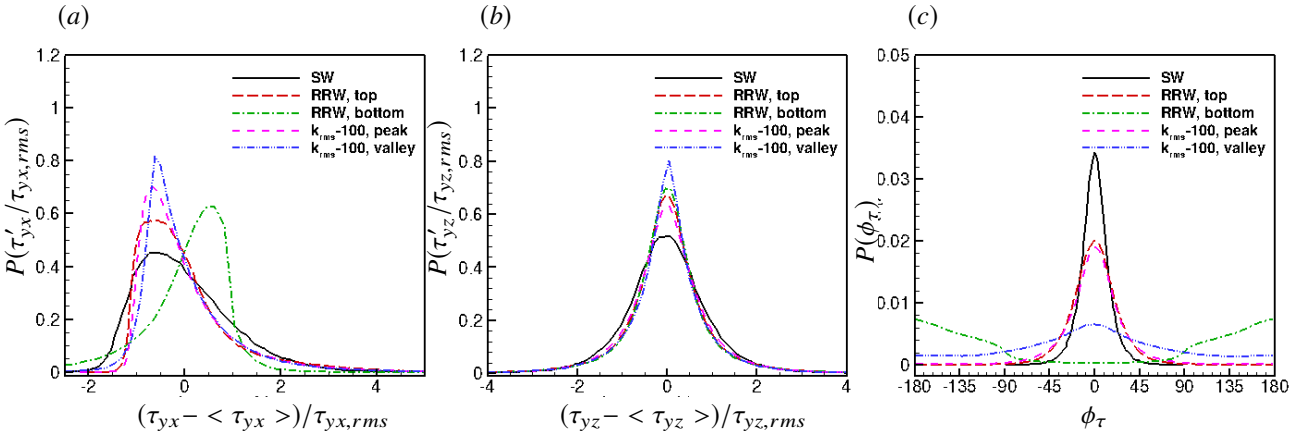

Fig. 11 Case RRW and Case $k_{rms}-100$ compared to Case SW at $Re_\tau = 400$: (a) PDF of streamwise shear-stress fluctuations, normalized by the rms value; (b) PDF of spanwise shear-stress fluctuations, normalized by the rms value; (c) PDF of the angle formed between the shear-stress vector and the streamwise direction.

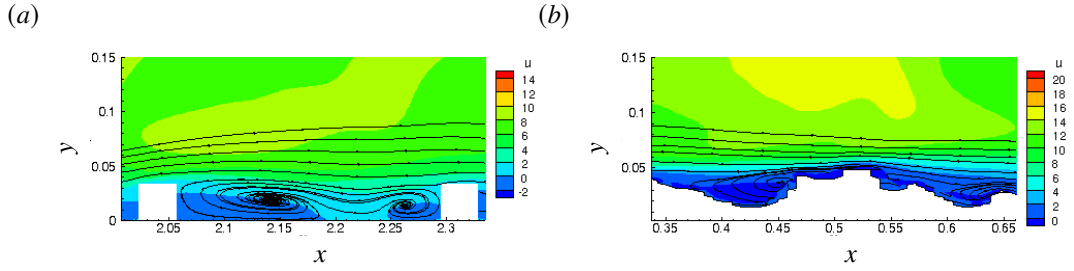

Fig. 12 Streamwise velocity fields and streamline pattern in the vicinity of the roughness elements: (a) Case RRW; (b) Case $k_{rms}-100$.

2. Joint PDF distribution of wall shear stress

To further investigate the effect of roughness on wall shear-stress fluctuations, Fig. 13 shows the joint PDF of the wall shear-stress vector magnitude and the yaw angle for smooth wall, rod-roughened wall, and random-rough wall. The joint PDF of Case SW in Fig. 13(a) shows a similar contour map as Diaz-Daniel et al. [7]. They found that the probability of events with very small shear-stress magnitude $||\tau||$ can be neglected, and the probability is maximum when the shear-stress vector is parallel to the flow direction. A completely different distribution can be seen for Case RRW, as shown in Fig. 13(b). First, the probability of events with small shear-stress magnitude is not negligible, supporting the view that the very small streamwise fluctuations τ_{yx} can be associated with very small spanwise fluctuations τ_{yz}. Second, the maximum probability occurs at a very large yaw angle close to 180°, which corresponds to the events that large, negative streamwise fluctuations τ_{yx} are associated with small values of spanwise fluctuations τ_{yz}. These results are pertinent to the fact that the recirculation zones are strong between two adjacent rods within a cavity. Moreover, for Case SW when the yaw angle is between 20°and 40°, the probability of high magnitude events exhibits a sharp decrease. In contrast, a similar trend is observed in Case RRW. Case $k_{rms} - 100$ also presents interesting features in Fig. 13(c). First, the events with very low shear-stress magnitude have a higher probability, covering the range from small yaw angle (0°) to large yaw angle (180°). This indicates that the yaw angle between streamwise and spanwise fluctuations for small shear-stress magnitude are more evenly distributed. Second, the maximum probability occurs when the yaw angle is zero, similar to Case SW, however, it shifts to a smaller shear-stress magnitude. Additionally, the distribution maintains similar features with Case SW when $|\phi_\tau|$ is small, but is spread over a larger shear-stress magnitude.

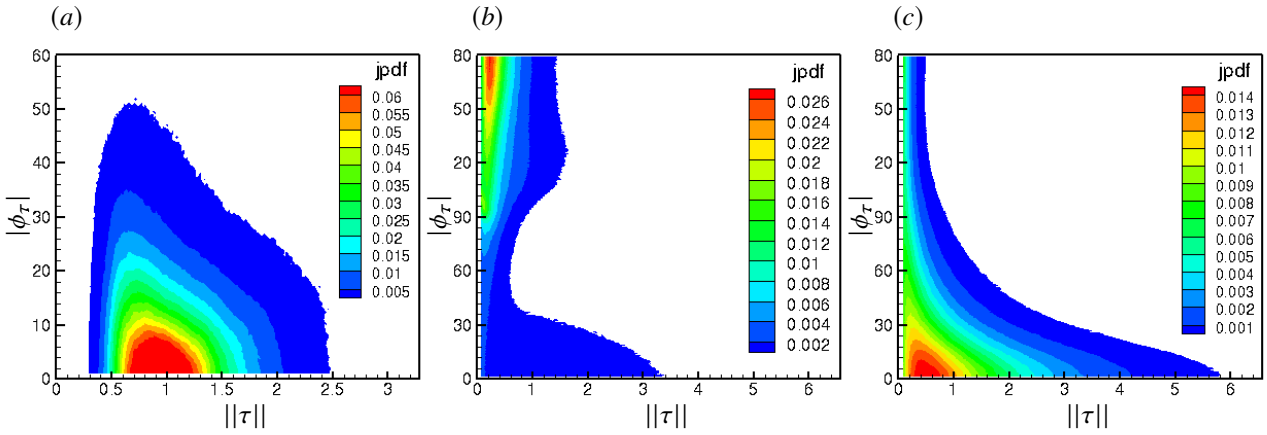

Fig. 13 Two-dimensional probability density function of the norm and yaw angle of the wall shear-stress vector at $Re_\tau = 400$: (a) Case SW; (b) Case RRW; (c) Case $k_{rms} - 100$.

In order to obtain a better understanding of the joint PDF distribution for the rough cases, the results are investigated based on separate regions. As shown in Fig. 14 (a), the joint PDF distribution of wall shear stress on the top surface of rods has a similar shape with the smooth wall. However, the probability is higher for both large yaw angle and large magnitude than Case SW. The maximum probability at large $|\phi_\tau|$ in Fig. 14(b) indicates a reverse flow in the cavity. Combining these two distributions can give us an explanation of the overall result in Fig. 13(b). For Case $k_{rms} - 100$, Fig. 14(c) shows that the peak region has a higher probability for events with small magnitude and large yaw angle. The results in the valley region imply that the events with low shear-stress magnitude have a relatively even and higher probability for a wide range of yaw angle. As shown in Fig. 14(d), the highest probability is concentrated in the region of small shear-stress magnitude and small yaw angle. Combining the results in the peak and valley regions, we can conclude that the reverse flow is enhanced by the presence of valleys, however, they are not as strong as the recirculation zones between the rods within the cavity.

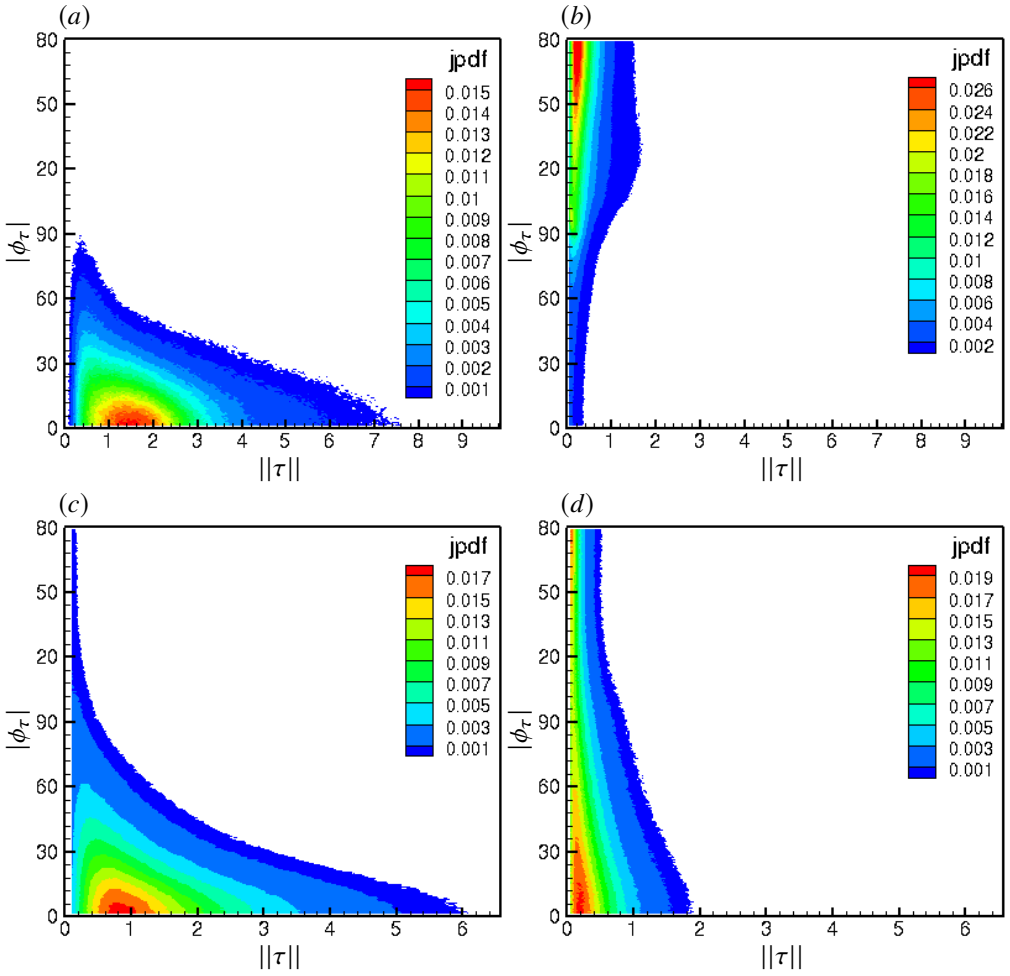

Fig. 14 Joint PDF distribution of the norm and yaw angle of the wall shear-stress vector for separate regions: (a) The top surface of the rods in Case RRW; (b) The bottom surface in the cavity in Case RRW; (c) The peak region in Case $k_{rms}-100$; (d) The valley region in Case $k_{rms}-100$.

V. Conclusion

We perform direct numerical simulation of turbulent channel flows to study the effects of random rough surface on the instantaneous flow field, turbulent statistics, momentum budget, and wall shear stress fluctuations. More low-velocity regions are observed near the rough wall and high-vorticity regions occur near the roughness asperities. The mean velocity profile exhibits a velocity deficit in the log-law region due to the presence of roughness. The peak of streamwise velocity fluctuations for the rough wall is decreased when scaled by the rough wall friction velocity. The pressure fluctuations are enhanced in the roughness sublayer, whereas the pressure fluctuations in the outer layer of the flow are not altered. The flow over a random rough surface maintains a similar MMB layer structure when compared to the smooth channel flow. The peak Reynolds stress location y_p denotes the transition from a balance between mean viscous force and mean effect of turbulent inertia to a balance between mean effect of turbulent inertia and mean advection. It is shown that the roughness causes the transition to occur closer to the wall when compared to a smooth case. We also investigate the statistics of wall shear stress fluctuations for rod-roughened and random rough channel flow. The relatively small mean values of streamwise shear-stress fluctuations are related to the fact that the grooves and valleys induce a reverse flow between roughness elements. The kurtosis of rough cases is larger than the smooth case, indicating the probability of extreme events is higher due to the roughness. The main feature of a rod-roughened case is that events with the maximum probability are at large shear-stress yaw angles. This is due to the pair of recirculating zones

within the cavity. The joint PDF distribution of the random rough case suggests that the probability of events with low shear-stress magnitude is not negligible. The events with larger shear-stress magnitude have a higher probability, which imply that the positive streamwise shear stress τ_{yx} is correlated with low spanwise shear stress τ_{yz}.

Acknowledgments

This work was supported by the United States Office of Naval Research (ONR) Grant N00014-17-1-2308 managed by Dr. Joe Gorski. Computing resources were provided by the Minnesota Supercomputing Institute (MSI). We are grateful to Prof. K. Flack at the United States Naval Academy for providing us with the scanned surface data used in the present work.

References

[1] Flack, K. A., and Schultz, M. P., "Review of hydraulic roughness scales in the fully rough regime," *Journal of Fluids Engineering*, Vol. 132, No. 4, 2010, p. 041203.

[2] Yuan, J., and Piomelli, U., "Estimation and prediction of the roughness function on realistic surfaces," *Journal of Turbulence*, Vol. 15, No. 6, 2014, pp. 350–365.

[3] Busse, A., Lützner, M., and Sandham, N. D., "Direct numerical simulation of turbulent flow over a rough surface based on a surface scan," *Computers & Fluids*, Vol. 116, 2015, pp. 129–147.

[4] Mehdi, F., Klewicki, J. C., and White, C. M., "Mean momentum balance analysis of rough-wall turbulent boundary layers," *Physica D: Nonlinear Phenomena*, Vol. 239, No. 14, 2010, pp. 1329–1337.

[5] Bhaganagar, K., Coleman, G., and Kim, J., "Effect of roughness on pressure fluctuations in a turbulent channel flow," *Physics of Fluids*, Vol. 19, No. 2, 2007, p. 028103.

[6] Meyers, T., Forest, J. B., and Devenport, W. J., "The wall-pressure spectrum of high-Reynolds-number turbulent boundary-layer flows over rough surfaces," *Journal of Fluid Mechanics*, Vol. 768, 2015, pp. 261–293.

[7] Diaz-Daniel, C., Laizet, S., and Vassilicos, J. C., "Wall shear stress fluctuations: Mixed scaling and their effects on velocity fluctuations in a turbulent boundary layer," *Physics of Fluids*, Vol. 29, No. 5, 2017, p. 055102.

[8] Khoo, B. C., Chew, Y. T., and Teo, C. J., "Near-wall hot-wire measurements," *Experiments in Fluids*, Vol. 31, No. 5, 2001, pp. 494–505.

[9] Mahesh, K., Constantinescu, G., and Moin, P., "A numerical method for large-eddy simulation in complex geometries," *J. Comput. Phys.*, Vol. 197, No. 1, 2004, pp. 215–240.

[10] Moser, R. D., Kim, J., and Mansour, N. N., "Direct numerical simulation of turbulent channel flow up to $Re_\tau = 590$," *Physics of Fluids*, Vol. 11, No. 4, 1999, pp. 943–945.

[11] Ashrafian, A., Andersson, H. I., and Manhart, M., "DNS of turbulent flow in a rod-roughened channel," *International Journal of Heat and Fluid Flow*, Vol. 25, No. 3, 2004, pp. 373–383.

[12] Barros, J. M., Schultz, M. P., and Flack, K. A., "Measurements of skin-friction of systematically generated surface roughness," *10th International Symposium on Turbulence and Shear Flow Phenomena (TSFP10), Chicago, USA*, 2017.

[13] Jeon, S., Choi, H., Yoo, J. Y., and Moin, P., "Space–time characteristics of the wall shear-stress fluctuations in a low-Reynolds-number channel flow," *Physics of Fluids*, Vol. 11, No. 10, 1999, pp. 3084–3094.